

This work was written as part of one of the author's official duties as an Employee of the United States Government and is therefore a work of the United States Government. In accordance with 17 U.S.C. 105, no copyright protection is available for such works under U.S. Law.

Public Domain Mark 1.0

<https://creativecommons.org/publicdomain/mark/1.0/>

Access to this work was provided by the University of Maryland, Baltimore County (UMBC) ScholarWorks@UMBC digital repository on the Maryland Shared Open Access (MD-SOAR) platform.

Please provide feedback

Please support the ScholarWorks@UMBC repository by emailing scholarworks-group@umbc.edu and telling us what having access to this work means to you and why it's important to you. Thank you.

Real-Time Processing Algorithms for Target Detection and Classification in Hyperspectral Imagery

Chein-I Chang, *Senior Member, IEEE*, Hsuan Ren, *Member, IEEE*, and Shao-Shan Chiang, *Student Member, IEEE*

Abstract—In this paper, we present a linearly constrained minimum variance (LCMV) beamforming approach to real time processing algorithms for target detection and classification in hyperspectral imagery. The only required knowledge for these LCMV-based algorithms is targets of interest. The idea is to design a finite impulse response (FIR) filter to pass through these targets using a set of linear constraints while also minimizing the variance resulting from unknown signal sources. Two particular LCMV-based target detectors, the constrained energy minimization (CEM) and the target-constrained interference-minimization filter (TCIMF), are presented. In order to expand the ability of the LCMV-based target detectors to classification, the LCMV approach is further generalized so that the targets can be detected and classified simultaneously. By taking advantage of the LCMV-based filter structure, the LCMV-based target detectors and classifiers can be implemented by a QR-decomposition and be processed line-by-line in real time. The experiments using HYDICE and AVIRIS data are conducted to demonstrate their real time implementation.

Index Terms—Classification, constrained energy minimization (CEM), linearly constrained minimum variance (LCMV), real time implementation, target-constrained interference-minimization filter (TCIMF), target detection.

I. INTRODUCTION

IN MANY practical applications, real-time implementation has the advantage of processing data online and provides timely analysis to resolve critical situations. The increasing need for real-time processing has been witnessed in signal and image processing areas such as the internet communications, web browsing, telemedicine, etc. In remote sensing applications, satellite imagery has been a major source used for study in ecology, geology, agriculture, global climate monitoring, etc., where there is no pressing need for real time processing. However, due to recent advances of remote sensing instrument technology, images acquired by high resolution airborne sensors, such as the 224-band airborne visible/infrared imaging spectrometer (AVIRIS) operated by NASA's Jet Propulsion Laboratory, Pasadena, CA, and the 210-band hyperspectral

digital imagery collection experiment (HYDICE) developed by the Naval Research Laboratory (NRL), Washington, DC, can now expand applications to law enforcement, battlefield, reconnaissance and surveillance, environmental monitoring, disaster and damage control, etc., where real-time processing becomes crucial and provides immediate assessment. In the past, many algorithms have been developed for multispectral/hyperspectral image processing. In order for them to implement in real time, a complete knowledge of image endmember signatures is generally required such as linear unmixing methods, Gaussian maximum likelihood (ML) approach. In addition, most of these algorithms are implemented on a single pixel basis and do not take advantage of sample-spectral correlation.

This paper presents intraline (i.e., line-by-line) real-time processing algorithms for target detection and classification in hyperspectral imagery where the only required knowledge is targets of interest. Besides, these algorithms make use of the sample correlation matrix to take into account the intraline, sample-spectral correlation (i.e., pixel correlation within a line). They are based on linearly constrained minimum variance (LCMV) beamforming approach proposed by Frost [1], [2]. The idea of these LCMV-based algorithms formulates an array of sensors used in an adaptive beamformer as a bank of spectral channels operated by a remote sensing instrument. The signals arriving from a desired direction in the sensor array are then viewed as desired targets present in an image pixel that is acquired simultaneously by the spectral channels. With this interpretation, an LCMV beamformer can be modified to an LCMV-based target detector that detects specific targets in a remotely sensed image [3]. Since the only required knowledge is targets of interest, this LCMV-based target detector can implement a finite impulse response (FIR) filter that linearly constrains these targets by specific gains while minimizing the variance resulting from unknown signal sources. Two significant advantages can benefit from the LCMV approach. First, it does not require the knowledge of natural background signatures or interferers in an image scene. Such unknown interference can be minimized at the filter output. Second, its filter structure can be implemented by systolic arrays using a QR decomposition [4], [5]. By taking these advantages, the LCMV-based designed target detector can be implemented as parallel processing algorithms in real time.

One disadvantage of the LCMV beamformer is the constraint that only locks on the direction of signal arrival and does not distinguish signals arriving from that particular direction. As a result, the LCMV-based algorithms can only be used for target

Manuscript received February 18, 2000; revised July 27, 2000. This work was supported by the Bechtel Nevada Corporation under Contract DE-AC08-96NV11718 through the Department of Energy.

C.-I Chang and S.-S Chiang are with the Remote Sensing Signal and Image Processing Laboratory, Department of Computer Science and Electrical Engineering, University of Maryland, Baltimore County, Baltimore, MD 21250 USA (e-mail: cchang@umbc.edu).

H. Ren is with U.S. Army Edgewood Chemical Biological Center, Aberdeen Proving Ground, MD 21010 USA.

Publisher Item Identifier S 0196-2892(01)02143-X.

detection and cannot discriminate the detected targets one from another. In order to resolve this problem, a new approach is proposed to augment the linear constraints in such a manner that the LCMV target detector can perform target classification as a classifier. Instead of using a constraint vector in the LCMV approach, a constraint matrix is introduced such that the detected targets can be classified in a single image by row vectors in the constraint matrix, while the column vectors can be used to detect targets as is done in the LCMV target detector. The experiments demonstrate that the derived LCMV classifier can not only detect targets of interest in real time, but also can classify them in a single image by displaying them in different colors for visualization.

The remainder of this paper is organized as follows. Section II describes the LCMV approach, from which LCMV-based target detectors can be derived. Section III extends the LCMV target detectors to LCMV target classifiers using a constraint matrix. Section IV presents real time implementation for the LCMV classifiers. In Section V, HYDICE and AVIRIS data experiments are used to illustrate how an LCMV classifier can detect as well as classify multiple targets simultaneously in a single image in real time. Finally, Section VI concludes some remarks.

II. LINEARLY CONSTRAINED MINIMUM VARIANCE (LCMV) TARGET DETECTOR

Assume that a remotely sensed image is a collection of image pixels denoted by $\{\mathbf{r}_1, \mathbf{r}_2, \dots, \mathbf{r}_N\}$, where $\mathbf{r}_i = (r_{i1}, r_{i2}, \dots, r_{iL})^T$ for $1 \leq i \leq N$ is an L -dimensional pixel vector, N is the total number of pixels in the image, and L is the total number of spectral channels. Suppose that $\{\mathbf{t}_1, \mathbf{t}_2, \dots, \mathbf{t}_k\}$ is a set of spectral signatures of k targets of interest present in the image. We form a target signature matrix, denoted by $\mathbf{T} = [\mathbf{t}_1 \mathbf{t}_2 \dots \mathbf{t}_k]$. The goal is to design a FIR linear filter with L filter coefficients $\{w_1, w_2, \dots, w_L\}$, denoted by an L -dimensional vector $\mathbf{w} = (w_1, w_2, \dots, w_L)^T$ that minimizes the filter output energy subject to the following constraint:

$$\mathbf{T}^T \mathbf{w} = \mathbf{c} \quad \text{where } \mathbf{t}_j^T \mathbf{w} = \sum_{l=1}^L t_{jl} w_l = c_j \text{ for } 1 \leq j \leq k \quad (1)$$

where $\mathbf{c} = (c_1, c_2, \dots, c_k)^T$ is a constraint vector.

Now let y_i denote the output of the designed FIR filter resulting from the input \mathbf{r}_i . Then y_i can be expressed by

$$y_i = \sum_{l=1}^L w_l r_{il} = \mathbf{w}^T \mathbf{r}_i = \mathbf{r}_i^T \mathbf{w}. \quad (2)$$

Using (1) and (2), the LCMV beamformer can be modified as an LCMV-based target detector in [3] by minimizing the average energy of the filter outputs

$$\begin{aligned} \frac{1}{N} \left[\sum_{i=1}^N y_i^2 \right] &= \frac{1}{N} \left[\sum_{i=1}^N (\mathbf{r}_i^T \mathbf{w})^T \mathbf{r}_i^T \mathbf{w} \right] \\ &= \mathbf{w}^T \left(\frac{1}{N} \left[\sum_{i=1}^N \mathbf{r}_i \mathbf{r}_i^T \right] \right) \mathbf{w} \\ &= \mathbf{w}^T \mathbf{R}_{L \times L} \mathbf{w} \end{aligned} \quad (3)$$

where $\mathbf{R}_{L \times L} = (1/N) [\sum_{i=1}^N \mathbf{r}_i \mathbf{r}_i^T]$ is the autocorrelation sample matrix of the image. This results in the following linearly constrained optimization problem:

$$\min_{\mathbf{w}} \{ \mathbf{w}^T \mathbf{R}_{L \times L} \mathbf{w} \} \text{ subject to } \mathbf{T}^T \mathbf{w} = \mathbf{c}. \quad (4)$$

The solution to (4) can be obtained in [1], [2] by

$$\mathbf{w}^* = \mathbf{R}_{L \times L}^{-1} \mathbf{T} (\mathbf{T}^T \mathbf{R}_{L \times L}^{-1} \mathbf{T})^{-1} \mathbf{c}. \quad (5)$$

It should be noted that the designed LCMV-based target detector obtained by (5) uses the sample correlation matrix $\mathbf{R}_{L \times L}$ to account for the second-order statistics in the image, which is sample-spectral correlation among $\{\mathbf{r}_1, \mathbf{r}_2, \dots, \mathbf{r}_N\}$. The second-order correlation is shown in the design of the optimal weight \mathbf{w}^* in (5), where $\mathbf{R}_{L \times L}^{-1}$ is the inverse of $\mathbf{R}_{L \times L}$.

Two special cases of (1) are of particular interest.

A. Constrained Energy Minimization (CEM)

If we are only interested in a single target d , that is, $\mathbf{T} = \mathbf{d}$, the constraint vector \mathbf{c} in (1) is then substituted by $\mathbf{d}^T \mathbf{w} = \sum_{l=1}^L d_l w_l = 1$ and becomes a constraint scalar. In this specific case, (3) is reduced to

$$\min_{\mathbf{w}} \{ \mathbf{w}^T \mathbf{R}_{L \times L} \mathbf{w} \} \text{ subject to } \mathbf{d}^T \mathbf{w} = 1 \quad (6)$$

with the optimal solution \mathbf{w}^* given by

$$\mathbf{w}^* = \frac{\mathbf{R}_{L \times L}^{-1} \mathbf{d}}{\mathbf{d}^T \mathbf{R}_{L \times L}^{-1} \mathbf{d}}. \quad (7)$$

The solution obtained by (7) was called constrained energy minimization (CEM) in [7], [8], and referred to as minimum variance distortionless response (MVDR) in adaptive beamforming [2], [4].

It is worth noting that the CEM target detector solved by (2) and (6) can be interpreted as an alternative form of the classical matched filter with the matched signal given by the \mathbf{w}^* in (7) [9]. More interestingly, if we assume that a complete knowledge of image endmembers is available and the corresponding end-member signature matrix \mathbf{M} can be divided into a desired signature \mathbf{d} and an undesired signature matrix \mathbf{U} , we can substitute the undesired signature annihilator $P_{\mathbf{U}}^{\perp} = [\mathbf{I} - (\mathbf{U}^T \mathbf{U})^{-1} \mathbf{U}^T]$ defined in [10] for $\mathbf{R}_{L \times L}^{-1}$ in (7). So, the resulting CEM target detector becomes an *a posteriori* orthogonal subspace projection (OSP) classifier, which was referred to as a signature subspace classifier (SSC) or oblique subspace classifier (OBC) in [10]. If we further discard the scale factor $(\mathbf{d}^T \mathbf{R}_{L \times L}^{-1} \mathbf{d})^{-1}$ in (7) and replace $\mathbf{R}_{L \times L}^{-1}$ with $P_{\mathbf{U}}^{\perp}$, the CEM target detector is simply reduced to the OSP classifier derived in [11]. A comparative performance analysis between the CEM target detector and the OSP-based classifiers can be found in [6]. Additionally, it has been shown in recent reports [12], [14] that under the Gaussian noise assumption, the Gaussian maximum likelihood (ML) classifier was equivalent to the OSP classifier. Therefore, only the OSP classifiers will be used in this paper for comparative study.

B. Target-Constrained Interference-Minimized Filter (TCIMF)

In many practical applications, the targets of interest can be categorized into two classes, one class of desired targets and another class of undesired targets. In this case, we can break

up the target signature matrix \mathbf{T} into a desired target signature matrix denoted by $\mathbf{D} = [\mathbf{d}_1 \mathbf{d}_2 \cdots \mathbf{d}_p]$, and an undesired target signature matrix denoted by $\mathbf{U} = [\mathbf{u}_1 \mathbf{u}_2 \cdots \mathbf{u}_q]$, i.e., $\mathbf{T} = [\mathbf{D} \mathbf{U}]$. In this case, we can design a FIR filter passing the desired targets by using a $p \times 1$ unit constraint vector

$$\mathbf{1}_{p \times 1} = \underbrace{(1, 1, \dots, 1)}_p^T$$

while annihilating the undesired targets by using a $q \times 1$ zero constraint vector

$$\mathbf{0}_{q \times 1} = \underbrace{(0, 0, \dots, 0)}_q^T.$$

In order to do so, the constraint equation specified by (1) is replaced by

$$[\mathbf{D} \mathbf{U}]^T \mathbf{w} = \begin{bmatrix} \mathbf{1}_{p \times 1} \\ \mathbf{0}_{q \times 1} \end{bmatrix}. \quad (8)$$

The resulting constrained optimization problem becomes

$$\min_{\mathbf{w}} \{ \mathbf{w}^T \mathbf{R}_{L \times L} \mathbf{w} \} \text{ subject to } [\mathbf{D} \mathbf{U}]^T \mathbf{w} = \begin{bmatrix} \mathbf{1}_{p \times 1} \\ \mathbf{0}_{q \times 1} \end{bmatrix} \quad (9)$$

with the optimal weight vector \mathbf{w}^* solved by

$$\mathbf{w}^* = \mathbf{R}_{L \times L}^{-1} [\mathbf{D} \mathbf{U}] ([\mathbf{D} \mathbf{U}]^T \mathbf{R}_{L \times L}^{-1} [\mathbf{D} \mathbf{U}])^{-1} \begin{bmatrix} \mathbf{1}_{p \times 1} \\ \mathbf{0}_{q \times 1} \end{bmatrix}. \quad (10)$$

The filter designed by using \mathbf{w}^* in (10) is called the target-constrained interference-minimized filter (TCIMF) [15], [16].

III. LINEARLY CONSTRAINED MINIMUM VARIANCE (LCMV) TARGET CLASSIFIER

The LCMV target detector described in Section II can detect the targets of interest in \mathbf{T} or the desired targets in \mathbf{D} by simultaneously passing these targets through the filter using the constraint (1) or (8). Unfortunately, it does not differentiate these detected targets. In order to expand the capability of the LCMV target detector as a classifier, we further augment the constraint vector \mathbf{c} in (1) to a constraint matrix \mathbf{C} . The idea is to use each column vector in \mathbf{C} to generate a weight vector to detect a desired target while each row vector in \mathbf{C} is used to classify the detected target using a preselected color for target discrimination. As a result, all the desired targets can be detected as well as classified in one single image using \mathbf{C} .

Assume that the size of the constraint matrix \mathbf{C} is $k \times m$ and denoted by $\mathbf{C} = [\mathbf{c}_1 \mathbf{c}_2 \cdots \mathbf{c}_m]_{k \times m}$. In this case, the weight vector \mathbf{w} in (1) is also expanded by an $L \times m$ weight matrix $\mathbf{W} = [\mathbf{w}_1 \mathbf{w}_2 \cdots \mathbf{w}_m]$, which is comprised of m weight vectors $\{\mathbf{w}_1, \mathbf{w}_2, \dots, \mathbf{w}_m\}$, and is represented by

$$\mathbf{T}^T \mathbf{W} = \mathbf{C}. \quad (11)$$

The constraint matrix \mathbf{C} plays a significant role in the LCMV target classifier and can be used for two purposes. One is to use each $k \times 1$ column vector \mathbf{c}_j for $1 \leq j \leq m$ to detect specific targets. Another is to use each row vector of \mathbf{C} to assign a particular color to the detected targets so as to achieve target classification.

Using the constraint matrix \mathbf{C} specified by (11), (4) can now be generalized to

$$\min_{\mathbf{w}} \{ \mathbf{w}^T \mathbf{R}_{L \times L} \mathbf{w} \} \text{ subject to } \mathbf{T}^T \mathbf{w} = \mathbf{C}. \quad (12)$$

The optimal solution $\mathbf{W}^* = [\mathbf{w}_1^* \mathbf{w}_2^* \cdots \mathbf{w}_m^*]$ to (12) can be obtained by

$$\mathbf{W}^* = \mathbf{R}_{L \times L}^{-1} \mathbf{T} (\mathbf{T}^T \mathbf{R}_{L \times L}^{-1} \mathbf{T})^{-1} \mathbf{C}. \quad (13)$$

The use of the weight matrix \mathbf{W}^* in (13) is twofold. It detects desired targets and at the same time, it also classifies targets with the pre-selected colors assigned by row vectors in the constraint matrix \mathbf{C} . More specifically, the column dimensionality of \mathbf{C} , m , specifies the number of colors to be used to classify targets, whereas, the row dimensionality of \mathbf{C} , k , is the number of desired targets needed to be classified. For the TCIMF target detector to be implemented as a classifier, we only have to substitute $\mathbf{T} = [\mathbf{D} \mathbf{U}]$ for the \mathbf{T} in (13).

To illustrate the above idea, assume that we are interested in classifying k targets into m classes. In this case, the constraint matrix given by (11) must have the size of $k \times m$, denoted by $\mathbf{C} = [\mathbf{c}_1 \mathbf{c}_2 \cdots \mathbf{c}_m]_{k \times m}$ where each of the column vectors \mathbf{c}_j has dimensionality, k for $1 \leq j \leq m$ and corresponds to the constraint vector of the LCMV target detector specified by (4). The row dimensionality of \mathbf{C} , m , is then used to classify the k targets into m classes. It should be noted that k is not necessarily equal to m . For example, if there are two targets, which belong to the same type of an object, but have different but similar spectral signatures, they must be classified into the same class. So in this case, $k < m$. On the other hand, if partial knowledge of natural background signatures is available, it generally present interference to target classification and can be considered as undesired signatures. The elimination of such interference can enhance target detection and classification by using TCIMF. In this case, these signatures will be assigned to one class for annihilation. This also results in that $k < m$. Since all the detected k targets must be classified into m distinct classes, it is impossible to show their classification results with gray levels in one image. In order to resolve this difficulty, we assign different colors to each of rows in the constraint matrix \mathbf{C} so that each color is used to specify one class of targets.

As an example, suppose that there are five targets, $\mathbf{t}_1, \mathbf{t}_2, \mathbf{t}_3, \mathbf{t}_4, \mathbf{t}_5$ which belong to four types of vehicles, denoted by V1 (\mathbf{t}_1), V2 ($\mathbf{t}_2, \mathbf{t}_3$), V3 ($\mathbf{t}_4, \mathbf{t}_5$), and two background signatures $\mathbf{t}_6, \mathbf{t}_7$ which may be available from partial knowledge and can be used to represent undesired signatures. In this case, $k = 7$ and $m = 4$. If we assume that red, green, blue, and black colors will be used to specify these four types of classes, then the target signature matrix can be formed by seven targets $\mathbf{T} = [\mathbf{t}_1 \mathbf{t}_2 \mathbf{t}_3 \mathbf{t}_4 \mathbf{t}_5 \mathbf{t}_6 \mathbf{t}_7]$, and the constraint matrix \mathbf{C} can be specified by

$$\mathbf{C} = [\mathbf{c}_1 \mathbf{c}_2 \mathbf{c}_3] = \begin{bmatrix} 1 & 0 & 0 & 0 & 0 & 0 & 0 \\ 0 & 1 & 1 & 0 & 0 & 0 & 0 \\ 0 & 0 & 0 & 1 & 1 & 0 & 0 \\ \underbrace{\quad}_{\text{red}} & \underbrace{\quad}_{\text{green}} & \underbrace{\quad}_{\text{green}} & \underbrace{\quad}_{\text{blue}} & \underbrace{\quad}_{\text{blue}} & \underbrace{\quad}_{\text{black}} & \underbrace{\quad}_{\text{black}} \end{bmatrix} \quad (14)$$

where $\mathbf{c}_1^T = (1, 0, 0, 0, 0, 0, 0)^T$, $\mathbf{c}_2^T = (0, 1, 1, 0, 0, 0, 0)^T$ and $\mathbf{c}_3^T = (0, 0, 0, 1, 1, 0, 0)^T$ are constraint vector to detect seven targets. The three colors, red, green, and blue are used to specify three types of vehicles: V1, V2, and V3, respectively, where the one in row 1 of \mathbf{c}_1 is used to detect \mathbf{t}_1 , the ones in rows 2 and 3 of \mathbf{c}_2 are used to detect \mathbf{t}_2 , \mathbf{t}_3 , and the ones in rows 4 and 5 of \mathbf{c}_2 are used to detect \mathbf{t}_4 , \mathbf{t}_5 . As noticed in (14), the rows 6 and 7 in \mathbf{C} (i.e., columns 6 and 7 in \mathbf{C}^T) are zero vectors, and they are used to eliminate background signatures \mathbf{t}_6 , \mathbf{t}_7 by being assigned to the black color. The reason we included background signatures in the above illustration was because in many practical applications, there is always some partial knowledge about background. In this case, we should take advantage of it. If there is no such knowledge available, the background signatures \mathbf{t}_6 , \mathbf{t}_7 in (14) would be absent. In this case, the \mathbf{t}_6 , \mathbf{t}_7 would be considered as unknown interferers rather than undesired signatures. It is worth noting that for visual discrimination, the colors chosen to classify targets should be as distinct as possible. Nevertheless, they can be arbitrary. More importantly, if a pixel is shown by a mixture of different colors, it may suggest that this particular pixel may be mixed by materials represented by these colors. Such information cannot be provided by the LCMV target detector.

IV. REAL TIME IMPLEMENTATION

One of advantages of the LCMV approach is that the correlation matrix $\mathbf{R}_{L \times L}$ in the optimal weights specified by (5), (10), and (13) can be decomposed into a product of a unitary matrix \mathbf{Q} and an upper triangular matrix \mathbf{R} by either the Givens rotations or the Householder transform. Such a decomposition is called *QR*-decomposition [4], [5]. By means of *QR*-decomposition, there is no need to compute the inverse of $\mathbf{R}_{L \times L}$, $\mathbf{R}_{L \times L}^{-1}$.

Suppose that data processing is carried out line-by-line from left to right and top to bottom. Let the image to be processed be denoted by a data matrix $[\mathbf{r}_{ti}]_{t=1, i=1}^{M, N}$ of size $M \times N$ where M is the number of lines (rows) and N is the total number of pixel vectors in one line (i.e., the number of columns in the image). Then for each line t , we form a data matrix $\mathbf{X}_t = [\mathbf{r}_{t1} \mathbf{r}_{t2} \cdots \mathbf{r}_{tN}]$ where \mathbf{r}_{ti} is the pixel vector being visited at time instance i in the t th line. In this case, the $\mathbf{R}_{L \times L}$ in (3) is replaced by the data autocorrelation matrix of line t in the image, denoted by \sum_t

$$\sum_t = \frac{1}{N} \left[\sum_{i=1}^N \mathbf{r}_{ti} \mathbf{r}_{ti}^T \right] = \frac{1}{N} [\mathbf{X}_t \mathbf{X}_t^T]. \quad (15)$$

Using a *QR*-decomposition the matrix, \mathbf{X}_t can be expressed by

$$\mathbf{X}_t = \mathbf{Q}_t \mathbf{R}_t. \quad (16)$$

Here, \mathbf{Q}_t is a unitary matrix with $\mathbf{Q}_t^{-1} = \mathbf{Q}_t^T$, and $\mathbf{R}_t = [\mathbf{R}_t^{upper}]$ is not necessarily of full rank, where $\mathbf{0}$ is a zero vector

$$\mathbf{R}_t^{upper} = \begin{bmatrix} * & * & \cdots & * \\ 0 & * & \cdots & * \\ \vdots & \ddots & \ddots & \vdots \\ 0 & \cdots & 0 & * \end{bmatrix}$$

is an upper triangular matrix, and $*$ in \mathbf{R}_t^{upper} is a nonzero element. From (16), the inverse of \sum_t can be computed as

$$\sum_t^{-1} = N (\mathbf{X} \mathbf{X}^T)^{-1} = N \{ (\mathbf{R}_t^{upper})^{-1} [(\mathbf{R}_t^{upper})^T]^{-1} \} \quad (17)$$

where the unitary matrix \mathbf{Q}_t is canceled out in (17) because $\mathbf{Q}_t^{-1} = \mathbf{Q}_t^T$. Substituting \sum_t^{-1} in (17) for $\mathbf{R}_{L \times L}^{-1}$ in (5) yields

$$\mathbf{w}^* = \{ (\mathbf{R}_t^{upper})^{-1} [(\mathbf{R}_t^{upper})^T]^{-1} \} \cdot \mathbf{T} (\mathbf{T}^T \{ (\mathbf{R}_t^{upper})^{-1} [(\mathbf{R}_t^{upper})^T]^{-1} \} \mathbf{T})^{-1} \mathbf{c}. \quad (18)$$

Since \mathbf{R}_t^{upper} is an upper triangular matrix, so is $(\mathbf{R}_t^{upper})^{-1}$. Therefore, (18) does not require us to compute $\mathbf{R}_{L \times L}^{-1}$. As a result, it can be realized by systolic array implementation [4] and implemented in real time processing. For details of the systolic array implementation, we refer to references [4], [17]–[19].

Several comments are noteworthy.

- 1) The matrix size of $\mathbf{R}_{L \times L}$ is always fixed at $L \times L$ where L is the number of bands, but its rank is determined by N , which is the number of sample vectors that form $\mathbf{R}_{L \times L}$. In general, $\mathbf{R}_{L \times L}^{-1}$ is not of full rank. In sensor array processing, N is generally assumed to be greater than L to prevent $\mathbf{R}_{L \times L}$ from being of ill-rank. A detailed study on this issue can be found in [6]. However, using a *QR*-decomposition, direct computation of $\mathbf{R}_{L \times L}^{-1}$ is not necessary, as shown in (18), where we only have to invert the upper triangular matrix \mathbf{R}_t^{upper} . So this problem can be resolved by *QR*-decomposition.
- 2) When the sample correlation matrix $\mathbf{R}_{L \times L}$ is formed by the entire image, it can only capture the global properties within the image. By contrast, if $\mathbf{R}_{L \times L}$ is formed by lines, it updates information on a line-by-line basis. As a result, it enables us to characterize local properties. Therefore, its performance is generally better than the one using global properties.
- 3) The CEM filter implemented by the above line-by-line real-time processing only uses line information up to the line currently being processed. It updates information line by line and only adds this new line information to the calculation of $\mathbf{R}_{L \times L}^{-1}$. It does not require us to recalculate the inverse of the sample correlation matrix when every time new line information comes in. For this reason, it can be viewed as a causal real-time line-by-line processing.

V. REAL-TIME PROCESSING EXPERIMENTS

In this section, two sets of hyperspectral data, HYDICE and AVIRIS images, were used for real-time processing experiments.

A. HYDICE Data Experiment

In order to illustrate how the LCMV classifier can be implemented as a real-time target detect and classifier, a HYDICE image scene of size 64×64 (band 30) shown in Fig. 1(a) is used for experiments where 15 panels are targets of interest and located in the center of the scene. The ground sampling distance is 1.5 m. In this case, $M = N = 64$. Fig. 1(b) provides the ground truth map that shows precise spatial locations of the panels. The

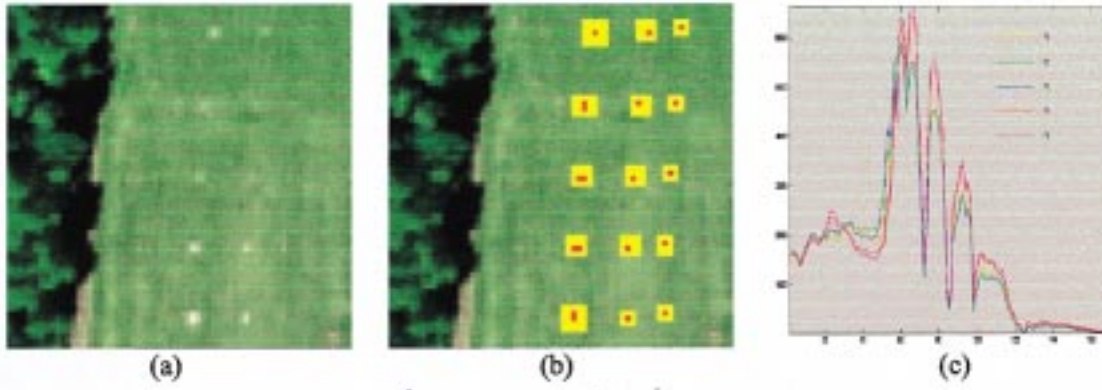


Fig. 1. (a) HYDICE image scene, (b) locations of 15 panels provided by ground truth, and (c) spectra of five signatures: P1, P2, P3, P4, and P5.

red pixels indicate the panel center pixels that were used to generate target signatures. The pixels in the yellow masks are considered to be panel pixels mixed with background pixels. These 15 target panels are arranged in a 5×3 matrix. Each element in this matrix is a square panel denoted by p_{ij} with row indexed by $i = 1, \dots, 5$ and column indexed by $j = a, b, c$. For each row $i = 1, \dots, 5$, the three panels p_{ia}, p_{ib}, p_{ic} were made from the same material but have three different sizes. For each column $j = a, b, c$, the five panels $p_{1j}, p_{2j}, p_{3j}, p_{4j}, p_{5j}$ are of the same size but were made from five different materials. The size of the panels in the first, second, and third columns are $3 \text{ m} \times 3 \text{ m}$, $2 \text{ m} \times 2 \text{ m}$, and $1 \text{ m} \times 1 \text{ m}$, respectively. Basically, these 15 panels have five different materials with three different sizes. The 1.5 m-spatial resolution of the image scene suggests that except for $p_{1a}, p_{2a}, p_{3a}, p_{4a}, p_{5a}$, which are two pixels in size, all the remaining panels are single pixels. Five panel signatures were generated by averaging the red center pixels in each row, denoted by P1, P2, P3, P4, and P5 with their spectra shown in Fig. 1(c). Five colors, red, green, white, yellow, and magenta, were selected to specify panels from row 1 to row 5, respectively. The choice of these colors is to make better visual discrimination among these 15 panels. For instance, instead of choosing traditional red, green, blue, we replaced blue color with white color because blue and green are visually close, and white makes a very good contrast. It is our preference and not necessarily the best. In this case, $k = m = 5$ and the constraint matrix \mathbf{C} in (11) is given by the 5×5 identity matrix

$$\mathbf{C} = [\mathbf{c}_1 \ \mathbf{c}_2 \ \mathbf{c}_3 \ \mathbf{c}_4 \ \mathbf{c}_5] = \begin{bmatrix} 1 & 0 & 0 & 0 & 0 \\ 0 & 1 & 0 & 0 & 0 \\ 0 & 0 & 1 & 0 & 0 \\ 0 & 0 & 0 & 1 & 0 \\ \underbrace{0}_{\text{red}} & \underbrace{0}_{\text{green}} & \underbrace{0}_{\text{white}} & \underbrace{0}_{\text{yellow}} & \underbrace{1}_{\text{magenta}} \end{bmatrix} \quad (19)$$

where the constraint vectors $\mathbf{c}_1, \mathbf{c}_2, \mathbf{c}_3, \mathbf{c}_4, \mathbf{c}_5$ in \mathbf{C} are used to detect and classify the 15 panels. Each column vector $\mathbf{c}_j = (c_{j1}, c_{j2}, c_{j3}, c_{j4}, c_{j5})^T$ specified by $c_{jj} = 1$ and $c_{ij} = 0$ for $i \neq j$ corresponds to the constraint in (8) with $\mathbf{d} = \mathbf{P}_j$ and $\mathbf{U} = [\mathbf{P}_i]_{i=1, i \neq j}^5$. Fig. 2(a)–(f) shows a sequence of images resulting from processing the image in Fig. 1(a) in real time using the TCIMF implemented by (10) with the optimal weight matrix

\mathbf{W}^* and the constraint matrix \mathbf{C} given by (13) and (19), respectively. For example, if we want to detect the panels in row 1, $c_{11} = 1$ in \mathbf{c}_1 is used to constrain $\mathbf{d} = [\mathbf{P}_1]$ and $c_{1j} = 0$ for $2 \leq j \leq 5$ in \mathbf{c}_1 to null $\mathbf{U} = [\mathbf{P}_2 \ \mathbf{P}_3 \ \mathbf{P}_4 \ \mathbf{P}_5]$ so that panels in row 1 can be detected while panels in other rows will be eliminated at the same time. The real-time processing was carried out line-by-line on a single pixel basis in a top-to-bottom and left-to-right fashion. When the entire image is used for processing, N is the total number of pixel vectors in the image. If the data is processed line-by-line, N is the total number of pixel vectors up to the line which is currently being visited by the CEM filter. Since the size of the HYDICE panel scene is 64×64 , the number of pixels in each line is $64 < 210$. In order to avoid singularity problem, the CEM filter uses the first four lines as its starting point to start its real-time processing. In the beginning of data processing, no panels were detected, so random colors were shown in the image in Fig. 2(a). As soon as the process detected the first target, i.e., the panel p_{1a} in row 1, the detected p_{1a} pixel was immediately changed to red, while the background became dark where the red color was chosen to specify the panels in row 1. Then the image remained unchanged shown in Fig. 2(b) until the process detected the p_{2a} panel pixel in row 2, where the pre-assigned green color was used to detect the panel p_{2a} and discriminate it from the red pixels that were panel pixels in row 1. Fig. 2(c) shows a complete detection process of the second row of panels. This process was continued to detect the third row of panels shown in Fig. 2(d) with the white color, the fourth row of panels shown in Fig. 2(e) with the yellow color and the fifth row of panels shown in Fig. 2(f) with the magenta color. At the time when the last pixel in the image was completed, the classification process was also accomplished and all the 15 panels were successfully classified by five colors, red for the panels in row 1, green for the panels in row 2, white for the panels in row 3, yellow for the panels in row 4, and magenta for the panels in row 5. In order to demonstrate how important to use a color map to visualize the classification result in Fig. 2(f), Fig. 2(g) shows only the gray scale image with all detected 15 panels. As we can from Fig. 2(g), there is no way to discriminate the panels of one row from the panels of another row.

Several experiments were also conducted by including some partial knowledge in the LCMV-based target classifier, for instance, grass and tree in the image scene. These two natural

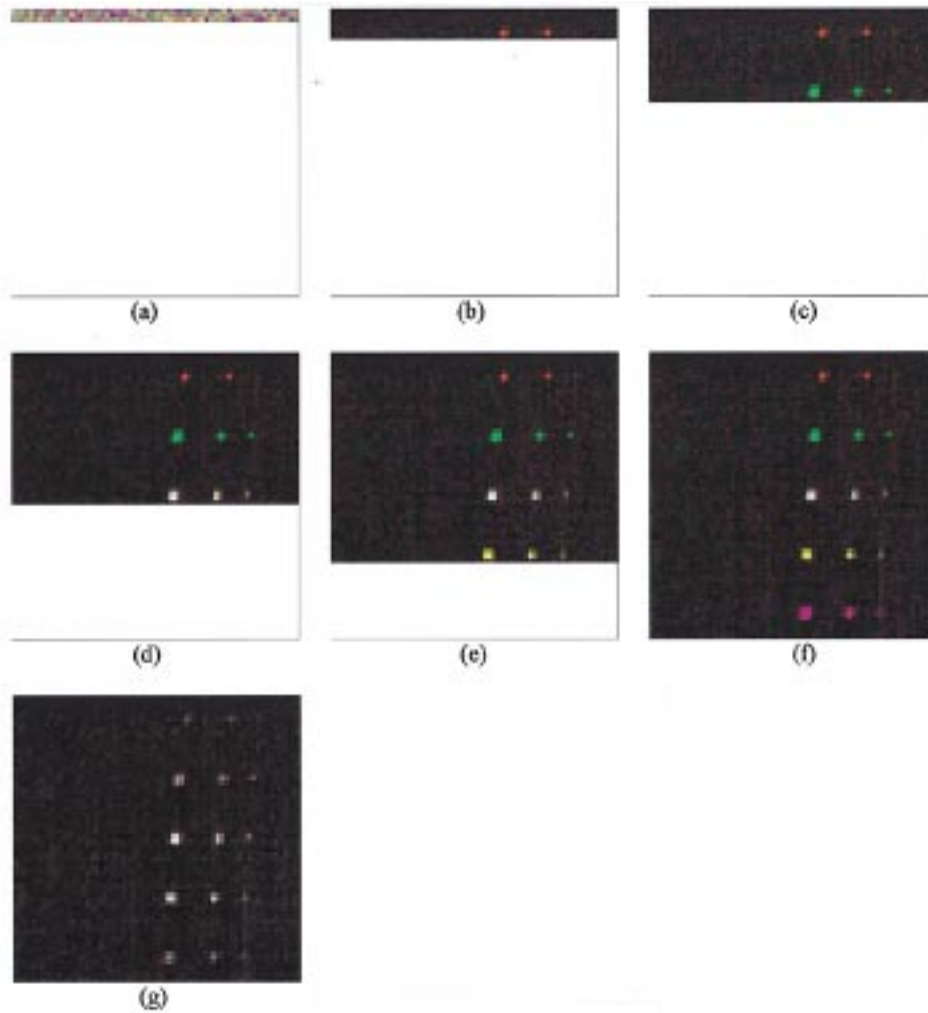


Fig. 2. (a) No panels detected, (b) detection of panels in row 1, (c) detection of panels in row 2, (d) detection of panels in row 3, (e) detection of panels in row 4, (f) detection of panels in row 5, and (g) detection results of 15 panels shown in a gray scale image.

TABLE I
DETECTION RESULTS OF THE TCIMF AND THE OSP CLASSIFIER USING 50%
ABUNDANCE AS A CUTOFF THRESHOLD VALUE

	TCIMF					OSP				
	N	N_R	N_{RD}	R_D	N_{FAP}	N	N_R	N_{RD}	R_D	N_{FAP}
P1	3	3	2	0.6667	0	3	3	1	0.6667	6
P2	3	4	3	0.7500	0	3	4	2	0.5000	338
P3	3	4	3	0.7500	0	3	4	3	0.7500	227
P4	3	4	3	0.7500	0	3	4	0	0.0000	443
P5	3	4	3	0.7500	0	3	4	3	0.7500	0
Total	15	19	14	0.7368	0	15	19	9	0.4737	1014

TABLE II
DETECTION RESULTS OF THE TCIMF AND THE OSP CLASSIFIER USING 25%
ABUNDANCE AS A CUTOFF THRESHOLD VALUE

	TCIMF					OSP				
	N	N_R	N_{RD}	R_D	N_{FAP}	N	N_R	N_{RD}	R_D	N_{FAP}
P1	3	3	2	1.0000	0	3	3	2	0.6667	35
P2	3	4	4	1.0000	0	3	4	4	0.5000	1572
P3	3	4	4	1.0000	0	3	4	4	1.0000	712
P4	3	4	4	1.0000	0	3	4	4	1.0000	2046
P5	3	4	3	0.7500	0	3	4	3	0.7500	13
Total	15	19	17	0.8947	0	15	19	17	0.8947	4378

background signatures can be used as undesired targets for background annihilation. The results not included here showed that

TABLE III
DETECTION RESULTS OF THE TCIMF AND THE OSP CLASSIFIER USING 20%
ABUNDANCE AS A CUTOFF THRESHOLD VALUE

	TCIMF					OSP				
	N	N_R	N_{RD}	R_D	N_{FAP}	N	N_R	N_{RD}	R_D	N_{FAP}
P1	3	3	3	1.0000	0	3	3	2	0.6667	51
P2	3	4	4	1.0000	1	3	4	4	1.0000	1879
P3	3	4	4	1.0000	0	3	4	4	1.0000	774
P4	3	4	4	1.0000	0	3	4	4	1.0000	2468
P5	3	4	4	1.0000	0	3	4	3	0.7500	21
Total	15	19	19	1.0000	1	15	19	17	0.8947	5193

there was not much improvement. This is because there are large fields of trees and grass in the image scene. It is impossible to generate a well-represented set for background signatures in the scene.

Since Fig. 1(b) provides a ground truth map, we can actually compare the performance of the TCIMF to that of the OSP classifier by tallying how many of 15 panel pixels are detected and also classified correctly. It should be noted that the images generated by the TCIMF and the OSP are abundance fractional images that are gray scale. In this case, we need a thresholding method to determine if a pixel is a panel pixel. The abundance percentage cutoff method proposed in [14] was used to threshold

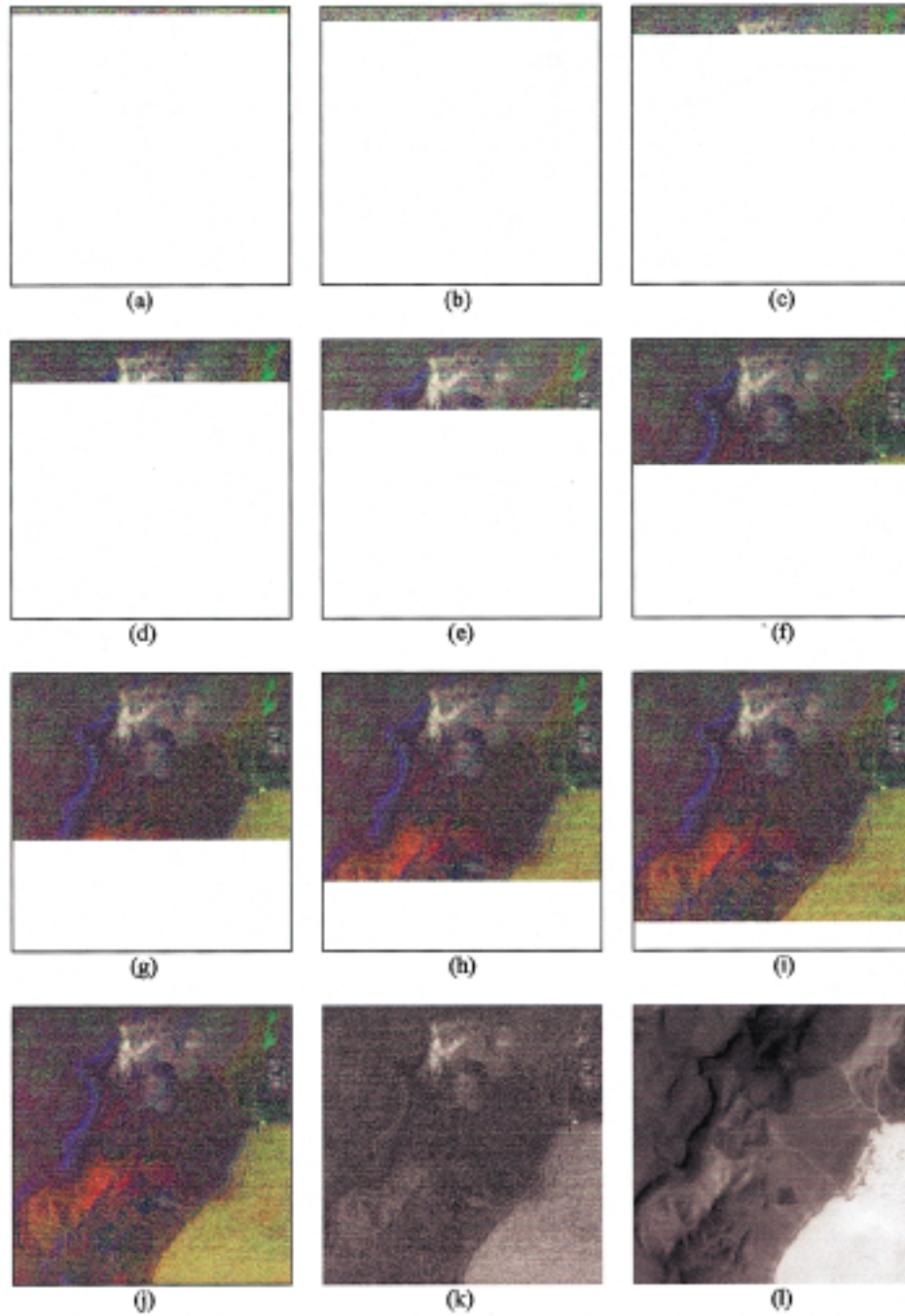


Fig. 3. (a) No panel detected with random colors, (b) vegetation detected with green, (c), (d) cinders detected with white, (e) shade detected with blue, (f) playa and an anomaly detected with olive, (g) rhyolite detected with red, (h), (i) no further targets detected, (j) color map of classification results, (k) detection results of 15 panels shown in a gray scale image, and (l) an AVIRIS image scene (band 30).

abundance fractional images into binary images. If the abundance fraction of the desired target signature present in a pixel is above a certain percentage, the pixel will be declared a target pixel and assigned to 1. Otherwise, the pixel will be considered to be a background pixel and assigned to 0. Tables I–III were detection results obtained by using 50%, 25%, and 20% abundance as cutoff threshold values, respectively, where N is total number of panel pixels, N_R is the number of red panel pixels, N_{RD} is the number of red panel pixels detected and classified correctly, N_{FAP} is the number of false alarm pixels, and R_D is the detection rate defined by $R_D = N_{RD}/N_R$. As shown

in these tables, the TCIMF performed significantly better than the OSP classifier. As the cutoff abundance percentage was decreased from 50% to 20%, the detection rates of the TCIMF and the OSP were improved at the expense of an increase in false alarm pixels. In Table II, when the 25% abundance was used as a cutoff threshold value, both the TCIMF and the OSP classifier reached the same detection rate (0.8947) with no false alarm pixels for the TCIMF and 4378 false alarm pixels for the OSP classifier. However, as the abundance percentage was further decreased to 20%, the TCIMF achieved a 100% detection rate with only one false alarm pixel resulting from P2, while the

OSP classifier still remained the same detection rate, 0.8947, but suffered from a significantly large number of false alarm pixels, 5193, an increase of 815 false alarm pixels resulting from 5% abundance reduction.

B. AVIRIS Data Experiment

The AVIRIS data used in the experiments were the same data considered in [10]. It is a subscene of 200×200 pixels extracted from the upper left corner of the Lunar Crater Volcanic Field (LCVF), Northern Nye County, NV, shown in Fig. 3(l) (band 30), where five signatures of interest in these images were demonstrated in [10], “red oxidized basaltic cinders,” “rhyolite,” “playa (dry lakebed),” “shade,” and “vegetation.” The ground sampling distance is 20 m. Fig. 3(a)–(k) shows a sequence of real time processing images that detected these five targets in different stages. It started with random colors with no target pixels detected in Fig. 3(a). Then it first detected the vegetation with green in Fig. 3(b), then cinders with white in Fig. 3(c) and (d), shade with blue in Fig. 3(e), playa with olive in Fig. 3(f), and finally, rhyolite with red in Fig. 3(g). Fig. 3(h)–(i) showed no further targets detected. Fig. 3(j) and (k) shows the color and gray scale images after the processing was completed. The color map in Fig. 3(j) offers an advantage that the gray scale image cannot provide, visual discrimination of different detected targets in one single image. For example, there was an anomaly detected and marked by an orange circle at the top edge of the lake. This anomaly has size of two pixels and is invisible by visual inspection from Fig. 3(l). It was also detected in [6], but its detection was missed in [10], [11] because the used OSP classifier was supervised. As we examined its color closely, it seemed to be a mixture of white and olive. This indicated that the anomaly could be mixed by cinders and playa. Obviously, such information cannot be provided by the gray scale image in Fig. 3(k).

VI. CONCLUSION

This paper presents LCMV-based real-time processing algorithms for target detection and classification in hyperspectral imagery. They can be implemented as the CEM target detector, the TCIMF target detector, and the LCMV classifier line-by-line in real-time processing while taking advantage of intraline, sample-spectral correlation. The CEM target detector is derived for a single target detection with only the desired target assumed to be known *a priori*. The TCIMF target detector is further developed to enhance the detectability of the CEM target detector if undesired targets are also known by partial knowledge or can be obtained by unsupervised means. Since the LCMV beamforming approach is developed by locking on the direction of signal arrival, it cannot be used to discriminate multiple signals arriving from the desired direction. As a result, the CEM and the TCIMF target detectors cannot classify the multiple targets. In order to extend their ability to target classification, the constraint vector used in the LCMV beamforming formulation is augmented to a constraint matrix, which results in an LCMV classifier. The experimental results show that the LCMV-classifier not only can effectively detect multiple targets but also can classify

them in a single image using different colors. Most importantly, these two tasks can be accomplished by a line-by-line real-time process. The real-time processing capability of the LCMV classifier results from the LCMV beamforming structure that can be implemented by a QR decomposition. Although the experiments only demonstrate line-by-line implementation, the new developed LCMV classifier can be also implemented in pixel-by-pixel, array-by-array, or block-by-block real-time processing. In particular, a similar idea applied to the RX algorithm [20], [21] for anomaly detection is currently under investigation [22].

ACKNOWLEDGMENT

The authors would like to thank Dr. J.C. Harsanyi for providing the AVIRIS data.

REFERENCES

- [1] O. L. Frost III, “An algorithm for linearly constrained adaptive array processing,” *Proc. IEEE*, vol. 60, pp. 926–935, 1972.
- [2] B. D. Van Veen and K. M. Buckley, “Beamforming: A versatile approach to spatial filtering,” *IEEE Acoust., Speech, Signal Processing Mag.*, pp. 4–24, Apr. 1988.
- [3] C.-I. Chang and H. Ren, “Linearly constrained minimum variance beamforming for target detection and classification in hyperspectral imagery,” in *Int. Geoscience and Remote Sensing Symp.* '99, vol. 28, Hamburg, Germany, July 1999, pp. 1241–1243.
- [4] S. Haykin, *Adaptive Filter Theory*, NJ: Prentice-Hall, 1986, ch. 10.
- [5] G. H. Golub and G. F. Van Loan, *Matrix Computations*, 2nd ed. Baltimore, MD: John Hopkins Univ., 1989.
- [6] C.-I. Chang and D. Heinz, “Subpixel spectral detection for remotely sensed images,” *IEEE Trans. Geosci. Remote Sensing*, vol. 38, pp. 1144–1159, May 2000.
- [7] J. C. Harsanyi, “Detection and classification of subpixel spectral signatures in hyperspectral image sequences,” Ph.D. dissertation, Dept. Elect. Eng., Univ. Maryland, Baltimore County, Baltimore, Aug. 1993.
- [8] J. C. Harsanyi, W. Farrand, and C.-I. Chang, “Detection of subpixel spectral signatures in hyperspectral image sequences,” in *Annu. Meeting, Proc. American Society of Photogrammetry and Remote Sensing*, Reno, NV, 1994, pp. 236–247.
- [9] H. V. Poor, *An Introduction to Signal Detection and Estimation*, 2nd ed. New York: Springer-Verlag, 1994.
- [10] C.-I. Chang, X. Zhao, M. L. G. Althouse, and J.-J. Pan, “Least squares subspace projection approach to mixed pixel classification in hyperspectral images,” *IEEE Trans. Geosci. Remote Sensing*, vol. 36, pp. 898–912, May 1998.
- [11] J. C. Harsanyi and C.-I. Chang, “Hyperspectral image classification and dimensionality reduction: An orthogonal subspace projection,” *IEEE Trans. Geosci. Remote Sensing*, vol. 32, pp. 779–785, July 1994.
- [12] J. J. Settle, “On the relationship between spectral unmixing and subspace projection,” *IEEE Trans. Geosci. Remote Sensing*, vol. 34, pp. 1045–1046, July 1996.
- [13] C.-I. Chang, “Further results on relationship between spectral unmixing and subspace projection,” *IEEE Trans. Geosci. Remote Sensing*, vol. 36, pp. 1030–1032, May 1998.
- [14] C.-I. Chang and H. Ren, “An experiment-based quantitative and comparative analysis of hyperspectral target detection and image classification algorithms,” *IEEE Trans. Geosci. Remote Sensing*, vol. 38, pp. 1044–1063, Mar. 2000.
- [15] H. Ren and C.-I. Chang, “A target-constrained interference-minimized filter for subpixel target detection and classification in hyperspectral imagery,” in *Proc. Int. Geoscience and Remote Sensing Symp. 2000*, Honolulu, HI, July 24–28, 2000.
- [16] —, “Target-constrained interference-minimized approach to subpixel target detection for hyperspectral imagery,” *Opt. Eng.*, vol. 39, pp. 3138–3145, Dec. 2000.
- [17] C.-F. T. Tang, C.-I. Chang, and Y. J. Chen, “A minimum variance distortionless response beamformer with systolic array implementation,” in *Proc. Int. Conf. Signal Processing '90*, Beijing, Oct. 22–26, 1990, pp. 1109–1112.

- [18] C.-I Chang and M. L. G. Althouse, "A systolic array algorithm and architecture of adaptive spatial filters for FLIR target detection," in *IEEE Workshop on Visual Signal Processing and Communications*, Hsinchu, Taiwan, R.O.C., June 6–7, 1991, pp. 110–115.
- [19] C. R. Ward, P. J. Hargrave, and J. G. McWhirter, "A novel algorithm and architecture for adaptive digital beamforming," *IEEE Trans. Antennas Propagat.*, vol. AP-34, pp. 338–346, Mar. 1986.
- [20] I. S. Reed and X. Yu, "Adaptive multiple-band CFAR detection of an optical pattern with unknown spectral distribution," *IEEE Trans. Acoust., Speech, Signal Processing*, vol. 38, pp. 1760–1770, Oct. 1990.
- [21] C. M. Stellman, C. M. , G. G. Hazel, F. Bucholtz, J. V. Michalowicz, A. Stocker, and W. Scaaf, "Real-time hyperspectral detection and cuing," *Opt. Eng.*, vol. 39, pp. 1928–1935, July 2000.
- [22] C.-I Chang, S.-S. Chiang, and I. W. Ginsberg, "Anomaly detection in hyperspectral imagery," in *SPIE Conf. Geo-Spatial Image and Data Exploitation*, Orlando, FL, Apr. 2001.



Chein-I Chang (S'81–M'87–SM'92) received the B.S. degree from Soochow University, Taipei, Taiwan, R.O.C., in 1973, the M.S. degree from the Institute of Mathematics, National Tsing Hua University, Hsinchu, Taiwan, in 1975, and the M.A. degree from the State University of New York, Stony Brook, in 1977, all in mathematics. He also received the M.S. and M.S.E.E. degrees from the University of Illinois, Urbana, in 1982, and the Ph.D. degree in electrical engineering from the University of Maryland, College Park, in 1987.

He has been with the University of Maryland, Baltimore County (UMBC), Baltimore, as a Visiting Assistant Professor from January 1987 to August 1987, Assistant Professor from 1987 to 1993, and has been an Associate Professor in the Department of Computer Science since 1993. He was a Visiting Research Specialist in the Institute of Information Engineering, National Cheng Kung University, Tainan, Taiwan, from 1994 to 1995. He has a patent on automatic pattern recognition and several pending patents on image processing techniques for hyperspectral imaging and detection of microcalcifications. He is currently on the editorial board of *Journal of High Speed Networks* and is the Guest Editor of a special issue of that journal on telemedicine and applications. His research interests include automatic target recognition, multispectral/hyperspectral image processing, medical imaging, information theory and coding, signal detection and estimation, and neural networks.

Dr. Chang is a member of SPIE, INNS, Phi Kappa Phi, and Eta Kappa Nu.



Hsuan Ren (S'98–M'01) received the B.S. degree in electrical engineering from the National Taiwan University, Taipei, Taiwan, in 1994, and the M.S. and Ph.D. degrees, all in electrical engineering, from University of Maryland, Baltimore County, in 1998 and 2000, respectively.

He is currently on National Research Council (NRC) Associateship and supported by U.S. Army Edgewood Chemical Biological Center as a Postdoctor Fellow. He has two patents pending on hyperspectral target detection and image classification.

He is also a Visiting Assistant Professor in the University of Maryland, Baltimore County. His research interests include data compression, signal and image processing and pattern recognition.

Dr. Ren was a finalist of the student paper prize competition at IEEE Geoscience and Remote Sensing Symposium, Seattle, WA, in 1998 and won the third Paper Prize in the Student Paper Prize competition at IEEE Geoscience and Remote Sensing Symposium, Hawaii, in 2000. He is a member of Phi Kappa Phi.



Shao-Shan Chiang (S'98) received the B.S. degree from National Chengchi University, Taipei, Taiwan, in 1988, and the M.S. degree from National Taiwan University, Taipei, in 1990, both in mathematics. He is currently pursuing the Ph.D. degree in the Department of Computer Science and Electrical Engineering, University of Maryland, Baltimore County (UMBC), Baltimore.

He was a Software Engineer from 1992 to 1996 in Taipei. From 1996 to 1998, he was a Research Assistant in the Anesthesiology Research Laboratory,

UMBC. Since 1999, he has been a Research Assistant with the Remote Sensing Signal and Image Processing Laboratory, UMBC. His research interests include signal processing, pattern recognition, and remote sensing image processing.

Mr. Chiang is a member of SPIE.